

Nanoscale

Accepted Manuscript



This is an *Accepted Manuscript*, which has been through the Royal Society of Chemistry peer review process and has been accepted for publication.

Accepted Manuscripts are published online shortly after acceptance, before technical editing, formatting and proof reading. Using this free service, authors can make their results available to the community, in citable form, before we publish the edited article. We will replace this *Accepted Manuscript* with the edited and formatted *Advance Article* as soon as it is available.

You can find more information about *Accepted Manuscripts* in the [Information for Authors](#).

Please note that technical editing may introduce minor changes to the text and/or graphics, which may alter content. The journal's standard [Terms & Conditions](#) and the [Ethical guidelines](#) still apply. In no event shall the Royal Society of Chemistry be held responsible for any errors or omissions in this *Accepted Manuscript* or any consequences arising from the use of any information it contains.

Time-dependent Evolution of $\text{Bi}_{3.64}\text{Mo}_{0.36}\text{O}_{6.55}/\text{Bi}_2\text{MoO}_6$ Heterostructure for Enhanced Photocatalytic Activity *via* the Interfacial Hole Migration

Cite this: DOI: 10.1039/x0xx00000x

Zan Dai,^a Fan Qin,^a Huiping Zhao,^a Fan Tian,^a Yunling Liu^b and Rong Chen^{*a}

Hierarchical $\text{Bi}_{3.64}\text{Mo}_{0.36}\text{O}_{6.55}/\text{Bi}_2\text{MoO}_6$ isotype heterostructures were successfully prepared *via* a one-pot hydrothermal route by using Bi_2O_3 porous nanospheres as a sacrificial template. By tuning the reaction time, the formation process of $\text{Bi}_{3.64}\text{Mo}_{0.36}\text{O}_{6.55}/\text{Bi}_2\text{MoO}_6$ heterostructure involving Mo etching, phase transition and anisotropic growth were clearly clarified. More importantly, $\text{Bi}_{3.64}\text{Mo}_{0.36}\text{O}_{6.55}/\text{Bi}_2\text{MoO}_6$ heterostructure displayed remarkably enhanced photocatalytic activity for dye photodegradation than pure phase bismuth molybdate due to the efficient electron-holes separation and the interfacial photogenerated hole migration from inside $\text{Bi}_{3.64}\text{Mo}_{0.36}\text{O}_{6.55}$ layer to outside Bi_2MoO_6 layer. The opposite hole migration from outer layer to inner layer was also detected in $\text{Bi}_2\text{O}_3/\text{Bi}_2\text{WO}_6$ heterostructures, which resulted in the decrease of photocatalytic activity, further verifying the importance of hole migration direction. This work provides a novel route to fabricate heterostructured photocatalyst, as well as gives a strategy for mediating the charge migration to improve photocatalytic performance.

Received (will be filled in by the editorial staff),
Accepted (will be filled in by the editorial staff)

DOI: 10.1039/x0xx00000x

www.rsc.org/

Introduction

Visible-light-response photocatalysts for organic pollutants degradation and water splitting have drawn significant research interests in the past years due to the growing environmental concerns and limited utilization of solar energy.¹⁻⁴ Subsequently, various bismuth-based semiconductor materials have been explored as potential efficient photocatalysts for targeted photocatalytic reactions,⁵⁻⁷ especially Aurivillius phase compounds with layered structure.⁸⁻¹¹ Among them, Bi_2MoO_6 is undoubtedly a well-known photocatalyst for water splitting and organic dyes degradation, which possesses unique layered structures, narrow band gap and visible-light-response property.^{12,13} However, the application of Bi_2MoO_6 is currently limited by its low overall efficiency due to its rapid electron-hole recombination, slow carrier migration, and poor surface chemistry. Therefore, how to improve electron-hole separation efficiency of Bi_2MoO_6 to meet the requirement of visible-light-response photocatalytic application is still a big challenge.

Generally, morphology and structure regulating,¹⁴ doping with

proper elements,^{15,16} and building complex nanocomposites^{17,18} are considered as effective strategies to enhance photocatalytic efficiency of semiconductor materials. In particular, heterostructured photocatalysts with superior photocatalytic performance to single-component photocatalysts have received more and more attention. The build-in potential gradient at the interface of heterostructured composite could mediate the band structure, facilitate the efficient charge separation and subsequently reduce the chance of electron-hole pair recombination.¹⁹⁻²² For example, $\text{Bi}_2\text{MoO}_6/\text{TiO}_2$ and $\text{Bi}_2\text{MoO}_6/\text{ZnTiO}_3$ heterostructures exhibit enhanced visible light photocatalytic activity toward RhB degradation because of the synergistic effect of excellent charge separation characteristics.^{23,24}

Besides, heterostructured photocatalyst which contains the same elements but different phases also displays huge potential to enhance photocatalytic activity.^{25,26} For instance, the combination of cubic phase $\text{Bi}_{3.64}\text{Mo}_{0.36}\text{O}_{6.55}$ and orthorhombic phase Bi_2MoO_6 *via* n-n junction was reported.²⁷ However, the interface of composite heterostructure is significantly important because it is the key pathway to connect with different components. Therefore, simultaneously building heterostructure and regulating morphology would further improve the mobility of electrons and holes between different phases. Unfortunately, it has been rarely investigated. Motivated by these concerns and our previous work, we developed a facile time-dependent evolution hydrothermal route to construct hierarchical $\text{Bi}_{3.64}\text{Mo}_{0.36}\text{O}_{6.55}/\text{Bi}_2\text{MoO}_6$ heterojunctions from porous Bi_2O_3 nanospheres. By varying the reaction time, the heterostructure formation mechanism involving Mo etching, phase

^a Key Laboratory for Green Chemical Process of Ministry of Education and School of Chemistry and Environmental Engineering, Wuhan Institute of Technology, Xiongchu Avenue, Wuhan, 430073, PR China E-mail: rchenhku@hotmail.com, Fax: (+86)2787195680.

^b State Key Laboratory of Inorganic Synthesis and Preparative Chemistry, College of Chemistry, Jilin University, Changchun 130012, PR China.

† Electronic supplementary information available. See DOI: 10.1039/c000000x/

transition and anisotropic growth process was investigated. To understand the significantly enhanced visible-light-driven photocatalytic ability of $\text{Bi}_{3.64}\text{Mo}_{0.36}\text{O}_{6.55}/\text{Bi}_2\text{MoO}_6$ heterostructure, systematical characterization were employed to investigate the band structures, optical and electrochemical properties, separation and transfer of photogenerated electron-hole pairs of $\text{Bi}_{3.64}\text{Mo}_{0.36}\text{O}_{6.55}/\text{Bi}_2\text{MoO}_6$ heterojunctions, as well as the generation of reactive species during photocatalytic process.

Experimental

Materials

Bismuth nitrate pentahydrate ($\text{Bi}(\text{NO}_3)_3 \cdot 5\text{H}_2\text{O}$) and sodium tungstate dihydrate ($\text{Na}_2\text{WO}_4 \cdot 2\text{H}_2\text{O}$) were purchased from Aladdin (Shanghai, China). Poly (vinylpyrrolidone) (PVP, Mw=10,000) was purchased from Aldrich (USA). Sodium molybdate ($\text{Na}_2\text{MoO}_4 \cdot 2\text{H}_2\text{O}$), ethylene glycol (EG), urea, nitric acid (HNO_3), mannitol and rhodamin B (RhB) were obtained from Sinopharm Chemical Reagent Co. (China). All the reagents were analytical grade and used directly without further purification.

Synthesis

Bi_2O_3 nanospheres were synthesized by following the procedure of our reported literature.²⁸ In the typical synthesis, 0.0242 g $\text{Na}_2\text{MoO}_4 \cdot 2\text{H}_2\text{O}$ (0.1 mmol) were dissolved in 5 mL mannitol solution (0.1 M), and mixed with 5 mL mannitol suspension containing 0.05g prepared Bi_2O_3 nanospheres at room temperature. Then, the mixture was transferred into a stainless steel autoclave with Teflon liner to perform hydrothermal process at 150°C for 6 h. The obtained product was collected after centrifugation and washing with deionized water for five times. Finally, the sample was dried in a desiccator for further characterization (**BMO-2**). Other samples were prepared under identical experimental conditions by varying reaction time to 3 h (**BMO-1**) and 12 h (**BMO-3**), respectively. $\text{Bi}_2\text{O}_3/\text{Bi}_2\text{WO}_6$ heterostructure and Bi_2WO_6 nanospheres were prepared *via* the same hydrothermal procedure by using $\text{Na}_2\text{WO}_4 \cdot 2\text{H}_2\text{O}$ as tungsten precursor in aqueous solution at different reaction time (6 h for $\text{Bi}_2\text{O}_3/\text{Bi}_2\text{WO}_6$ and 18 h for Bi_2WO_6 , respectively).

Characterizations

The composition and crystal phase of obtained samples were characterized by powder X-ray diffraction (XRD, Bruker axS D8 Discover) with Cu K α radiation of 1.5406 Å. The morphology and structure of obtained samples were characterized by scanning electron microscope (SEM, Hitachi S4800) operating at 5.0 kV and transmission electron microscope (TEM, Philips Tecnai G2 20) operating at 200 kV. UV-vis diffuse reflectance spectra (DRS) were recorded on a UV-vis spectrometer (Shimadzu UV-2550) by using BaSO_4 as a reference and were converted from reflection to absorbance by the Kubelka-Munk method. Brunauer-Emmett-Teller (BET) specific surface area was analyzed by nitrogen adsorption on a Micromeritics ASAP 2020 nitrogen adsorption apparatus (USA). X-ray photoelectron spectra (XPS) were performed on a VG Multilab2000 spectrometer by using Al K α

(1486.6 eV) radiation as the source. Photoluminescence spectra (PL) were detected with a Shimadzu RF-5301PC fluorescence spectrophotometer. Raman spectra were recorded by using a Horiba Jobin-Yvon LabRam HR800 Raman microspectrometer, with an excitation laser at 320 nm.

Photocatalytic activity test

The photocatalytic activities of **BMO** samples were evaluated by the photocatalytic degradation of RhB under visible light irradiation of 500 W Xe lamp with a 420 nm cutoff filter (Beijing Changtuo). In a typical photocatalytic experiment, 0.05 g photocatalyst was dispersed in 100 mL RhB solution (10^{-5} mol/L) under magnetic stirring. The suspension was stirred in the dark for 1 h to ensure an adsorption-desorption equilibrium before irradiation. Then, the suspension was exposed to visible light irradiation under stirring. At each given time interval, 3 mL suspension was sampled and centrifuged to remove the solid photocatalyst. The concentration of dyes during the degradation was monitored by colorimetry using a Shimadzu UV2800 spectrophotometer. All the photocatalytic reactions were carried out at room temperature.

Photoelectrochemical Experiments

The photocurrent measurement, electrochemical impedance spectroscopy (EIS) measurement, and Mott-Schottky measurement were performed on a CHI660E electrochemistry workstation (Shanghai, China) at room temperature. All the experiments were carried out in a standard three-electrode cell containing 0.5 mol/L Na_2SO_4 aqueous solution with a platinum foil and a saturated calomel electrode as the counter electrode and the reference electrode, respectively. To prepare working electrodes, ITO glass were ultrasonically cleaned in soap-suds, deionized water and acetone, successively. The electrodes were prepared by mixing a slurry containing 80% as-prepared photocatalyst, 10% dimethylformamide (DMF) and 10% nafion on ITO glass and then dried in the air at 60 °C for 6 h. The area of electrodes is about $1 \times 1 \text{ cm}^2$. A 500W Xe lamp with a 420 nm cut off filter was used as light source.

Results and discussion

Figure 1a shows the XRD patterns of the products obtained at different hydrothermal reaction time (3, 6 and 12 h). It was observed that the product obtained after 3 h hydrothermal treatment (**BMO-1**) could be well indexed to cubic $\text{Bi}_{3.64}\text{Mo}_{0.36}\text{O}_{6.55}$ (JCPDS 43-446). With the reaction prolonging to 6 h, the characteristic diffraction peaks of the sample was assigned to two different crystal phase which was corresponding to cubic phase $\text{Bi}_{3.64}\text{Mo}_{0.36}\text{O}_{6.55}$ (JCPDS 43-446) and orthorhombic Bi_2MoO_6 (JCPDS 76-2388), respectively (**BMO-2**). No additional impurity phase was found in this diffraction pattern, indicative of the formation of $\text{Bi}_{3.64}\text{Mo}_{0.36}\text{O}_{6.55}/\text{Bi}_2\text{MoO}_6$ composites. As the reaction time further increases, the intensity of diffraction peaks of cubic-phase $\text{Bi}_{3.64}\text{Mo}_{0.36}\text{O}_{6.55}$ gradually decrease, whereas the intensity of Bi_2MoO_6 diffraction peaks increase, as shown in Figure S1 (ESI†).

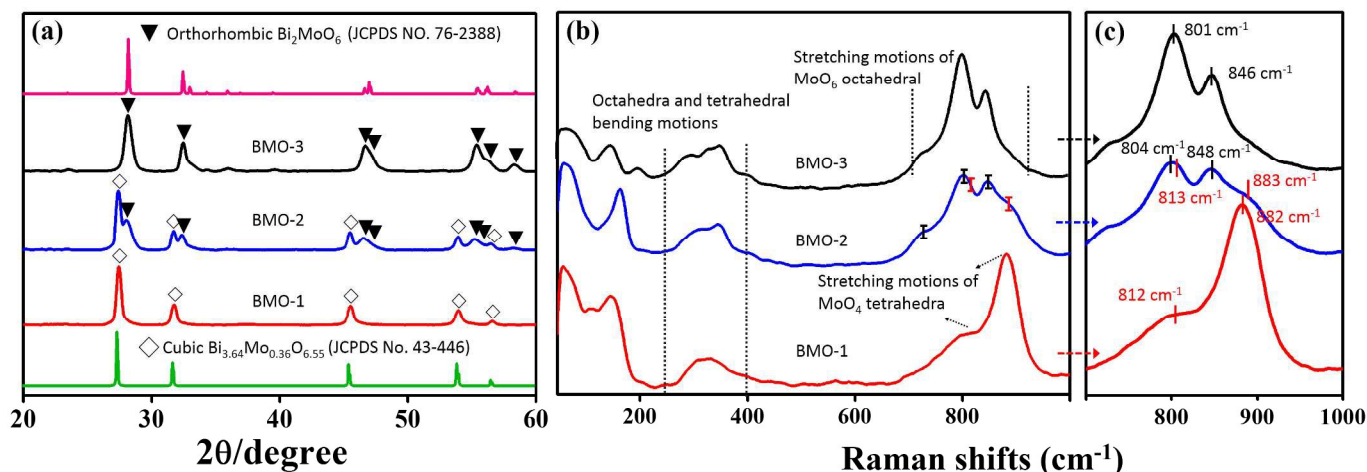


Fig. 1 XRD patterns (a) and Raman spectra (b and c) of **BMO** samples obtained at different reaction time.

After 12 h hydrothermal treatment, pure orthorhombic Bi_2MoO_6 was obtained, demonstrating the complete phase transition from $\text{Bi}_{3.64}\text{Mo}_{0.36}\text{O}_{6.55}$ to Bi_2MoO_6 .

Raman spectra was also utilized to provide the useful structure information for obtained **BMO** samples. Figure 1b displays the Raman spectra evolution of **BMO** samples obtained at different reaction time. Three characteristic bands at 882, 812 and 317 cm^{-1} were observed in the spectrum of $\text{Bi}_{3.64}\text{Mo}_{0.36}\text{O}_{6.55}$ (**BMO-1**), which could be assigned to Mo–O stretching motions and O–Mo–O bending motions of $[\text{MoO}_4]$ tetrahedral species.²⁹ The

distinguish peaks at 846, 801, and 735 cm^{-1} in the Raman spectrum of Bi_2MoO_6 (**BMO-3**) correspond to the stretching motions of distorted $[\text{MoO}_6]$ in Bi_2MoO_6 .³⁰⁻³³ It is worth noting that both $[\text{MoO}_4]$ and $[\text{MoO}_6]$ species could be observed in the Raman spectrum of $\text{Bi}_{3.64}\text{Mo}_{0.36}\text{O}_{6.55}/\text{Bi}_2\text{MoO}_6$ (**BMO-2**), indicative of the coexistence of $\text{Bi}_{3.64}\text{Mo}_{0.36}\text{O}_{6.55}$ and Bi_2MoO_6 phase. Compared with pure Bi_2MoO_6 and $\text{Bi}_{3.64}\text{Mo}_{0.36}\text{O}_{6.55}$, slight peak shift of stretching motions of $[\text{MoO}_6]$ octahedron and $[\text{MoO}_4]$ tetrahedron were observed in the spectrum of **BMO-2**, owing to the change of chemical environment in $\text{Bi}_{3.64}\text{Mo}_{0.36}\text{O}_{6.55}/\text{Bi}_2\text{MoO}_6$ heterostructure

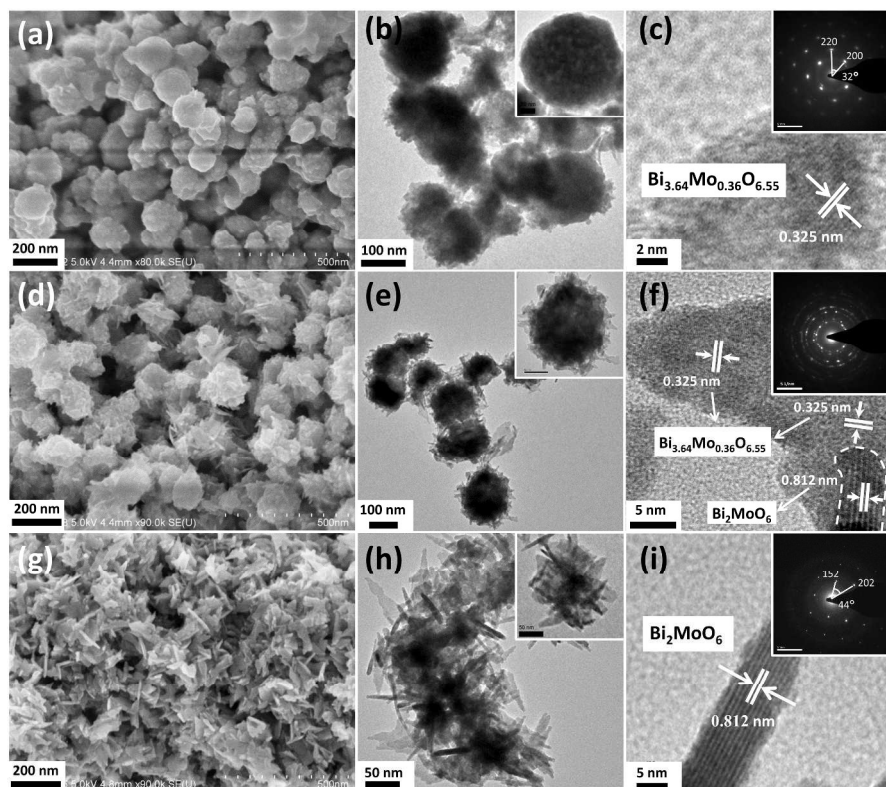


Fig. 2 SEM, TEM, HRTEM images and SAED patterns (inset) of **BMO** samples obtained at different reaction time: **BMO-1** (a-c), **BMO-2** (d-f) and **BMO-3** (g-i).

and the interaction of the two components (Figure 1c).

The morphology and structure of the as-synthesized **BMO** samples were investigated by SEM and TEM images, as shown in Figure 2. It demonstrates that sphere-like porous $\text{Bi}_{3.64}\text{Mo}_{0.36}\text{O}_{6.55}$ nanostructures were formed after 3 h solvothermal treatment (**BMO-1**). HRTEM image and SAED pattern reveal clear lattice fringe and diffraction spots, respectively, illustrating that the sample is well-crystallized. After 6 h reaction, the product mainly consists of large quantities of nanosheet-wrapped nanospheres, as depicted in Figure 2d. TEM image further demonstrates its spheric morphology and hierarchical structure with many nanosheets on the surface (Figure 2e). The corresponding HRTEM image of $\text{Bi}_{3.64}\text{Mo}_{0.36}\text{O}_{6.55}/\text{Bi}_2\text{MoO}_6$ nanocomposites reveals clear lattice fringe with d-spacing of 0.325 and 0.812 nm, which is corresponding to (111) crystallographic planes of cubic $\text{Bi}_{3.64}\text{Mo}_{0.36}\text{O}_{6.55}$ and (020) lattice plane of orthorhombic Bi_2MoO_6 , respectively (Figure 2f). The result confirms that a $\text{Bi}_{3.64}\text{Mo}_{0.36}\text{O}_{6.55}/\text{Bi}_2\text{MoO}_6$ composite with heterostructure was fabricated in this synthesis. Noticeably, Bi_2MoO_6 product obtained after 12 h solvothermal reaction presents a sheet-like morphology, which has an obvious aggregation tendency (Figure 2g). TEM image of Figure 2h further demonstrates its sheet-like morphology and structure. The lattice fringe and diffraction spots in HRTEM image and SAED pattern well match to single crystal Bi_2MoO_6 , as shown in Figure 2i.

XPS measurement was also performed to further confirm the formation of $\text{Bi}_{3.64}\text{Mo}_{0.36}\text{O}_{6.55}/\text{Bi}_2\text{MoO}_6$ heterostructures and investigate the chemical state of Bi and Mo in this heterostructure. Figure 3a shows full XPS spectra of as-prepared **BMO** samples, demonstrating that all the products were mainly composed of Bi,

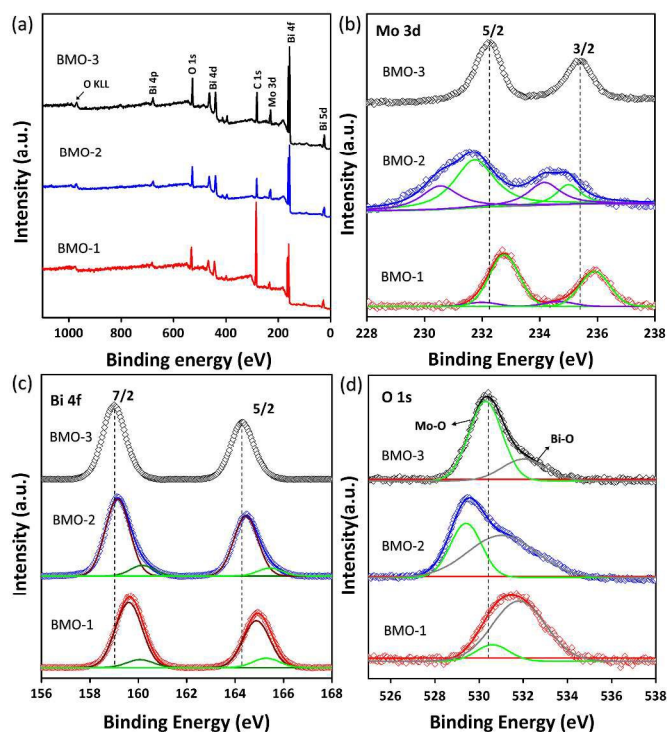
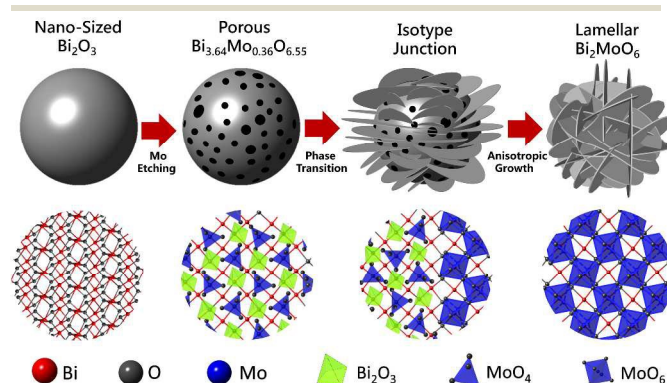


Fig. 3 Survey (a) and high-resolution Mo 3d (b), Bi 4f (c), and O 1s (d) XPS spectra of **BMO** samples.

Mo and O elements (C signal comes from the reference sample). In the high resolution Mo 3d XPS spectrum of **BMO-3** (Figure 3b), two peaks located at 232.3 and 235.4 eV could be assigned to $3d_{5/2}$ and $3d_{3/2}$ orbits, respectively, indicating that the chemical state of Mo^{6+} is presented in Bi_2MoO_6 .³⁴ Two new peaks appeared at 231.8 and 234.6 eV ascribed to Mo^{4+} were observed in high-resolution XPS spectrum of **BMO-1** after deconvolution, except for binding energy of Mo^{6+} . It is probably due to the difference of Mo coordination between the cubic and orthorhombic bismuth molybdate.^{35,36} More importantly, in the high-resolution Mo 3d XPS spectrum of **BMO-2**, all the peaks after deconvolution, which are corresponding to Mo^{+4} and Mo^{+6} , shift to lower binding energies due to the strong interaction between $\text{Bi}_{3.64}\text{Mo}_{0.36}\text{O}_{6.55}$ and Bi_2MoO_6 phase. The similar phenomenon was also observed in Bi 4f spectra of **BMO** samples (Figure 3c).³⁷ In addition, the location and relative intensity of the Mo-O (530.5 eV) and Bi-O (531.2 eV) peaks in **BMO-2** display obvious difference from that of **BMO-1** and **BMO-3**, indicating that the formation of heterojunction significantly influenced the environment of chemical bond in the crystal.

In addition, the Brunauer-Emmett-Teller (BET) specific surface areas of **BMO** samples were also investigated by N_2 adsorption-desorption measurements, as shown in Figure S2 (ESI[†]). The isotherms of all measured samples exhibit the characteristic of type IV with a hysteresis loop observed in the range of 0.60-1.00 P/P₀, suggesting their mesoporous properties. The calculated BET surface area (S_{BET}) are 20.3, 37.1 and 41.6 m^2g^{-1} for pure **BMO-1**, **BMO-2** and pure **BMO-3**, respectively.

Based on the observations, it was proposed that the evolution of composition, morphology and structure of bismuth molybdate could be regulated by reaction time *via* a hydrothermal method, involving Mo etching, phase transition and anisotropic growth process, as illustrated in Scheme 1. In the presence of acidic mannitol solution, Bi_2O_3 nanospheres were firstly etched by MoO_4^{2-} to form cubic phase $\text{Bi}_{3.64}\text{Mo}_{0.36}\text{O}_{6.55}$ nanospheres under hydrothermal treatment, which also presents a porous structure, as demonstrated by TEM image. In this stage, the Mo stoichiometry in the cubic $\text{Bi}_{3.64}\text{Mo}_{0.36}\text{O}_{6.55}$ phase is smaller than that of Bi_2MoO_6 , and synchronously reveals a higher bismuth content. Therefore, the composition of $\text{Bi}_{3.64}\text{Mo}_{0.36}\text{O}_{6.55}$ could be assumed to the Bi_2O_3 type phase in the form of $(\text{Bi}_{1-x}\text{Mo}_x)_2\text{O}_{3+\delta}\cdot\text{Bi}_2\text{O}_3$ ($x=0.18$), in which



Scheme 1 Illustration of $\text{Bi}_{3.64}\text{Mo}_{0.36}\text{O}_{6.55}/\text{Bi}_2\text{MoO}_6$ heterojunctions formation.

the Mo surrounding is tetrahedral.²⁹ With hydrothermal reaction prolonging, Mo and O gradually penetrate into $(\text{Bi}_{1-x}\text{Mo}_x)_2\text{O}_{3+\delta}\cdot\text{Bi}_2\text{O}_3$ phase, leading to the phase transition of known Bi-Mo-O system upon hydrothermal heating. In this case, Aurivillius 2D lamellar Bi_2MoO_6 nanosheets were generated. Furthermore, the phase transition became more and more pronounced with the increase of reaction time, as confirmed by the relatively diffraction peak intensity of $\text{Bi}_{3.64}\text{Mo}_{0.36}\text{O}_{6.55}$ and Bi_2MoO_6 in their corresponding XRD spectra (Figure S1, ESI†). A good homogeneity was noticed for the sample obtained after 12 h hydrothermal reaction (**BMO-3**), in accordance with XRD pattern and Raman spectrum, indicative of the presence of pure orthorhombic γ - Bi_2MoO_6 only.

Photocatalytic activities of the as-synthesized **BMO** samples were evaluated by RhB degradation under visible light irradiation. Before illumination, the dark adsorption over **BMO** samples were performed. As shown in Figure 4a, all the samples could reach adsorption-desorption equilibrium within 1 h, and only 10% RhB was absorbed. Compared with reported $\text{Bi}_{3.64}\text{Mo}_{0.36}\text{O}_{6.55}/\text{Bi}_2\text{MoO}_6$ heterostructure, it displays much faster adsorption-desorption equilibrium rate than that of reported $\text{Bi}_{3.64}\text{Mo}_{0.36}\text{O}_{6.55}/\text{Bi}_2\text{MoO}_6$ sample, which preforms overnight adsorption before illumination.²⁷ Figure 4b shows the variation of RhB concentration (C/C_0) with irradiation time over different **BMO** samples. For comparison, direct RhB photolysis and RhB photodegradation over commercial Degussa P25 and the mixture of equal amount **BMO-1** and **BMO-3** were also performed under identical conditions. It reveals that the direct photolysis of RhB under visible irradiation was negligible. Among the tested samples, heterostructured **BMO-2** exhibits the highest photocatalytic activity, which could completely decompose RhB within 2 h, as confirmed by the total organic carbon (TOC) results (Figure S3, ESI†). However, the RhB degradation efficiency over P25, **BMO-1** and **BMO-3** were only 62%, 39% and 83%, respectively, even after 4 h visible light irradiation. It is worth noticing that the mixture of **BMO-1** and **BMO-3** also displays much poorer photodegradation efficiency than that of **BMO-2** heterostructure. It further confirms that the improved photocatalytic performance of **BMO-2** is ascribed to the formation of heterojunction in $\text{Bi}_{3.64}\text{Mo}_{0.36}\text{O}_{6.55}/\text{Bi}_2\text{MoO}_6$ nanocomposites, rather than simply mixing the two components. In addition, the kinetics data of RhB photodegradation reaction over **BMO** samples fit to a pseudo-first-order model, as expressed by $\ln(C_0/C_t) = kt$, where C_0 and C_t represents the concentration of RhB before and after irradiation, t is irradiation time and k is the apparent rate constant. To exclude the effect of surface area, the values of apparent rate constant per unit surface area of the catalysts (k/S_{BET}) were used to evaluate the photocatalytic efficiency of **BMO** samples. It is reported that high k/S_{BET} value benefits to improving the photocatalytic efficiency.³⁸ The calculated k/S_{BET} values of **BMO-1**, **BMO-2** and **BMO-3** were 0.09, 0.42 and 0.19 $\text{m}^2 \cdot \text{h}^{-1}$, respectively (Figure 4c). It is found that the k/S_{BET} values of **BMO-2** is 2 times higher than that of **BMO-3**, although **BMO-3** possesses the highest BET surface area. From the viewpoint of applications, the chemical and physical stability of photocatalyst is of significant importance. Therefore, recycling photocatalytic experiments over heterostructured **BMO-2** sample were also

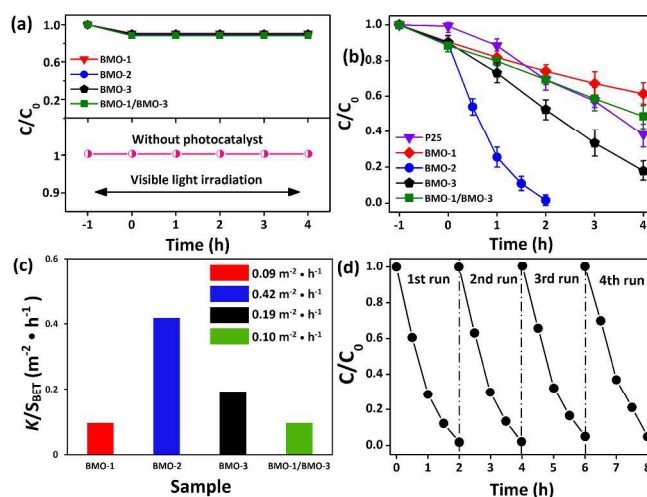


Fig. 4 Dark adsorption-desorption over **BMO** samples and direct photolysis in the absence of photocatalyst (a), photocatalytic RhB degradation (b) and pseudo-first-order kinetic constants per unit surface area (c) of **BMO** samples under visible light irradiation. Recycle RhB photodegradation results of **BMO-2** (d).

conducted. As shown in Figure 4d, **BMO-2** sample remains excellent photodegradation efficiency and its original morphology (Figure S4, ESI†) after four consecutive photodegradation cycles, implying that $\text{Bi}_{3.64}\text{Mo}_{0.36}\text{O}_{6.55}/\text{Bi}_2\text{MoO}_6$ heterojunction photocatalyst possesses favorable stability and no photocorrosion occurs during the photodegradation process.

To understand the reason of enhanced photocatalytic ability of $\text{Bi}_{3.64}\text{Mo}_{0.36}\text{O}_{6.55}/\text{Bi}_2\text{MoO}_6$ heterostructure, it is primarily important to identify the active species for the photodegradation of organic dyes. Therefore, we firstly performed trapping experiments by using tert-butyl alcohol (TBA, $\cdot\text{OH}$ radical scavenger), 1, 4-benzoquinone (BQ, $\cdot\text{O}_2^-$ radical scavenger), ammonium oxalate (AO, hole scavenger) and AgNO_3 (electron scavenger) to determine the major reactive species responsible for RhB oxidation over **BMO-2**. As shown in Figure S5 (ESI†), the photodegradation efficiency of RhB dramatically decreased with the addition of ammonium oxalate. However, only slightly decrease in photocatalytic activity of **BMO-2** were observed in the presence of TBA and BQ, illustrating that $\cdot\text{OH}$ and $\cdot\text{O}_2^-$ had little contribution to RhB photodegradation. The results illustrate that photogenerated holes are major active species involved in RhB photodegradation, which was further confirmed by the slight enhancement of RhB photodegradation after adding AgNO_3 to capture photogenerated electrons.

As the photogenerated holes were the dominate species in this photocatalytic reaction, the separation of photogenerated electron-hole pairs is of great importance. Photoluminescence (PL) spectra was used to investigate the separation efficiency of the photogenerated electron-hole pairs. As shown in Figure 5a, **BMO-2** heterostructure exhibits the lowest photoluminescence intensity than that of pure **BMO-1** and **BMO-3**, implying that $\text{Bi}_{3.64}\text{Mo}_{0.36}\text{O}_{6.55}/\text{Bi}_2\text{MoO}_6$ heterojunction could effectively suppress the recombination of electron-hole pairs, thus leading to

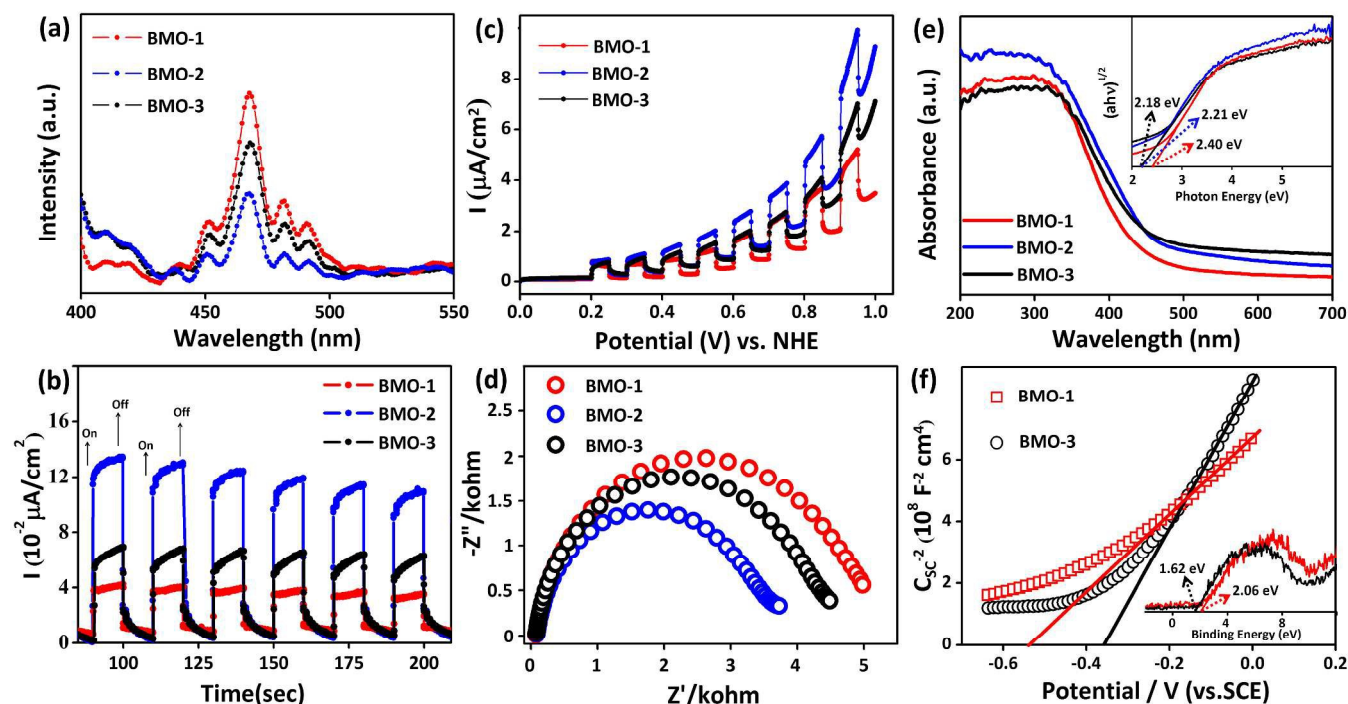


Fig. 5 Photoluminescence spectra (a), photocurrent response under visible light irradiation (b), linear sweep voltammograms (LSVs) under chopped visible light illumination (c), electrochemical impedance spectroscopy (d), UV-vis diffuse reflectance spectra and the plots of transformed Kubelka-Munk function versus light energy (inset) (e), Mott-Schottky plots and band XPS spectra (inset) (f) of **BMO** samples.

improved photocatalytic performance.³⁹ Subsequently, the photocurrent generation and EIS experiments were performed to investigate the electron excitation and the charge transport characteristics of **BMO** samples. It was found that photocurrent generated by **BMO-2** heterojunction was significantly higher than that of the pure **BMO-1** and **BMO-3** samples, suggesting that more photogenerated electrons were produced in $\text{Bi}_{3.64}\text{Mo}_{0.36}\text{O}_{6.55}/\text{Bi}_2\text{MoO}_6$ heterojunction under visible light irradiation (Figure 5b). The current-potential characteristics with a chopped light reveal the same results (Figure 5c). On the other hand, the smallest arc radius of the electrochemical impedance spectroscopy (EIS) Nyquist plot of **BMO-2** demonstrates the most fastest interfacial charge transference characteristics compared with pure **BMO** samples (Figure 5d), which favors the subsequent photocatalytic reactions.⁴⁰

On the basis of electrochemical characterizations and structure analysis, we proposed that the effective photogenerated electron-hole pairs separation and holes migration play a crucial role in the improved photocatalytic performance of **BMO-2** heterostructure. Figure 5e shows UV-vis diffuse reflectance spectroscopy of **BMO** samples. It is found that the absorption edges of **BMO** samples are around 350 to 450 nm and there is no significant difference in visible light region. The calculated band gap values is 2.40, 2.21 and 2.18 eV for **BMO-1**, **BMO-2** and **BMO-3** respectively. Based on Mott-Schottky plots of **BMO-1** and **BMO-3** (Figure 5f), the calculated flat band potential (V_{fb}) of **BMO-1** and **BMO-3** are -0.36 and -0.54 eV vs. $\text{Hg}/\text{Hg}_2\text{Cl}_2$, i.e., -0.12 and -0.30 eV vs. NHE, respectively. As an n-type semiconductor, the flat band potential is equal to its Fermi level. Generally, the bottom of the conduction

band (CB) of n-type semiconductor is more negative (about 0~0.2 eV) than Fermi level (i.e., the flat band potential), which is dependent on the electron effective mass and carrier concentration.^{41,42} Therefore, the E_{CB} of **BMO-1** and **BMO-3** are -0.32 and -0.50 eV vs. NHE, respectively, in this case. Accordingly, the valence band potential (E_{VB}) of **BMO-1** and **BMO-3** are 2.08 and 1.68 eV, respectively, based on the empirical formula ($E_g = E_{VB} - E_{CB}$). Band XPS spectra was also used to confirm the band structure, and the band potentials (2.06 eV for **BMO-1** and 1.62 eV for **BMO-3**) were consistent with the calculated results from Mott-Schottky plots (inset of Figure 5f). Therefore, the proposed pathway of photogenerated charge carriers transfer in $\text{Bi}_{3.64}\text{Mo}_{0.36}\text{O}_{6.55}/\text{Bi}_2\text{MoO}_6$ heterostructure should match the corresponding energy level.⁴³

In this heterojunction, photogenerated electrons easily transfer from the conduction band (CB) of Bi_2MoO_6 to the CB of $\text{Bi}_{3.64}\text{Mo}_{0.36}\text{O}_{6.55}$, whereas the photogenerated holes in the valence band (VB) of $\text{Bi}_{3.64}\text{Mo}_{0.36}\text{O}_{6.55}$ flow into the VB of Bi_2MoO_6 , resulting in facile separation of photogenerated charge carriers. More importantly, trapping experiment demonstrates that photogenerated holes are dominant species in the photodegradation of RhB. Hence, the hole migration from inner $\text{Bi}_{3.64}\text{Mo}_{0.36}\text{O}_{6.55}$ phase to Bi_2MoO_6 surface significantly promote the accumulation of holes on the surface of outside Bi_2MoO_6 , i.e. the reaction sites of RhB photodegradation, thus leading to enhanced photocatalytic efficiency.

To further verify the critical role of migration direction of photogenerated holes in photocatalysis, another heterostructured $\text{Bi}_2\text{O}_3/\text{Bi}_2\text{WO}_6$ nanospheres were also prepared from porous Bi_2O_3

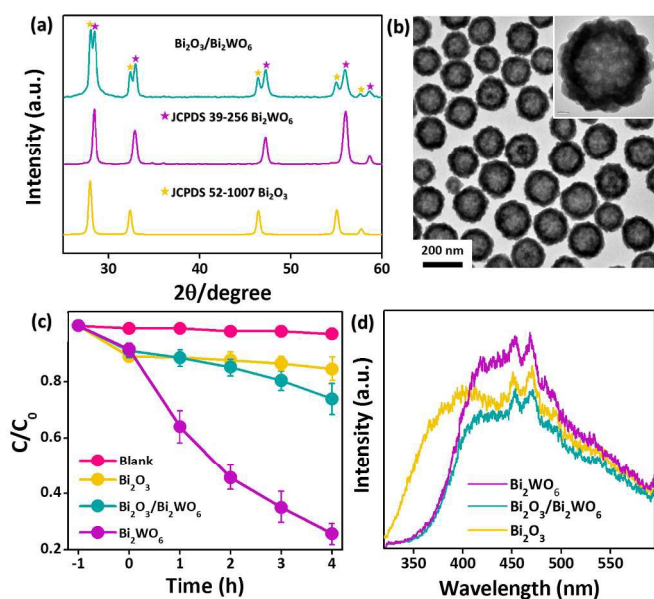
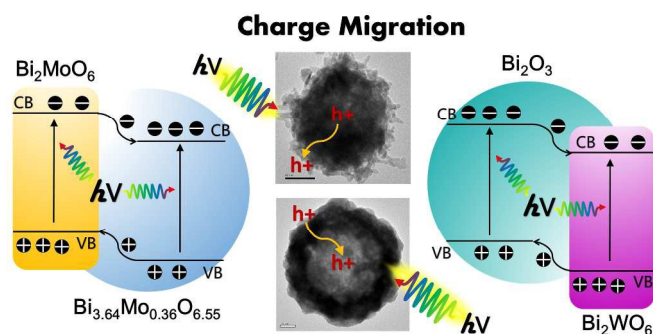


Fig. 6 XRD pattern (a) and TEM image (b) of Bi₂O₃/Bi₂WO₆ heterostructure. Photocatalytic RhB degradation efficiency (c) and photoluminescence spectra (d) of pure Bi₂O₃, Bi₂WO₆ and Bi₂O₃/Bi₂WO₆ heterostructure.

nanospheres. The obtained spheric Bi₂O₃/Bi₂WO₆ heterostructure was characterized by XRD pattern and TEM image, as shown in Figure 6a-b. As shown in Figure S6 (ESI[†]), it was found that Bi₂O₃/Bi₂WO₆ heterostructure presents similar morphology and particle size with pure Bi₂O₃ and Bi₂WO₆ nanospheres. In addition, it also possess similar BET surface area with Bi₂O₃ and Bi₂WO₆ nanospheres. Particularly, XPS analysis shows that the atomic ratio of Bi/W/O in Bi₂O₃/Bi₂WO₆ heterostructure (12.4:5.5:33.0) is close to stoichiometric value of Bi₂WO₆ (Figure S7, ESI[†]), illustrating that Bi₂WO₆ phase was the outer layer of Bi₂O₃/Bi₂WO₆ heterostructure. However, photocatalytic experiments show that Bi₂O₃/Bi₂WO₆ heterostructure exhibits much lower photocatalytic activity than that of pure Bi₂WO₆ nanospheres under visible light irradiation (Figure 6c). DRS spectra reveal that heterostructured Bi₂O₃/Bi₂WO₆ nanospheres display analogous light absorption in visible region (Figure S8, ESI[†]), compared with pure Bi₂WO₆ nanospheres. More importantly, PL spectra demonstrate that the fluorescence intensity of Bi₂O₃/Bi₂WO₆ heterostructure is obviously lower than that of pure Bi₂WO₆ nanospheres, indicating that the Bi₂O₃/Bi₂WO₆ heterojunction inhibits the electron-hole recombination (Figure 6d). Generally, it should have resulted in the improvement of photocatalytic performance. Nevertheless, opposite result was observed. The main reason is that the major reactive species, photogenerated holes, transferred from outside Bi₂WO₆ layer to inner Bi₂O₃ layer in the Bi₂O₃/Bi₂WO₆ p-n junction,⁴⁴ which hindered the photocatalytic reaction on the photocatalyst surface.

Therefore, a proposed pathway of photogenerated charge carriers transfer is summarized and illustrated in Scheme 2. Two kinds of photogenerated holes migration with opposite directions occur in



Scheme 2. Charge migration Bi_{3.64}Mo_{0.36}O_{6.55}/Bi₂MoO₆ and Bi₂O₃/Bi₂WO₆ heterostructure.

Bi_{3.64}Mo_{0.36}O_{6.55}/Bi₂MoO₆ n-n heterojunction and Bi₂O₃/Bi₂WO₆ p-n heterojunction, respectively, based on the matching of energy levels. It could significantly influence the photocatalytic reaction. If the photogenerated holes, the main reactive species in dye photodegradation, could transfer to the external of the heterostructure, to react with absorbed dye molecular, it might lead to the improvement of photocatalytic efficiency. In contrary, the holes migration from outer layer to inner phase results in the deficient contact between holes and dyes molecules, thus hindering the photocatalytic reaction.

Conclusions

In summary, hierarchical Bi_{3.64}Mo_{0.36}O_{6.55}/Bi₂MoO₆ heterostructures were synthesized by using porous Bi₂O₃ nanospheres as a sacrificial template *via* a facile hydrothermal method. The heterostructured Bi_{3.64}Mo_{0.36}O_{6.55}/Bi₂MoO₆ nanocomposite exhibits highly enhanced photocatalytic activity for RhB photodegradation than that of pure Bi_{3.64}Mo_{0.36}O_{6.55} and Bi₂MoO₆ due to the directed interfacial holes migration from inner layer to outer layer. The importance of hole migration direction was also verified by another Bi₂O₃/Bi₂WO₆ p-n heterostructure, which displayed an opposite hole migration from outer layer to inner layer, based on the corresponding energy level. This work provides a strategy for fabrication of heterostructured photocatalyst to realize the mediation of interfacial charges migration, thus promoting the photocatalytic efficiency.

Acknowledgements

This work was supported by the National Natural Science Foundation of China (21471121, 21171136), High-Tech Industry Technology Innovation Team Training Program of Wuhan Science and Technology Bureau (2014070504020243) and Open Research Fund of State Key Laboratory of Inorganic Synthesis and Preparative Chemistry (Jilin University, 2014-09).

Notes and references

- 1 A. Hagfeldt, M. Graetzel, *Chem. Rev.*, 1995, **95**, 49-68.
- 2 Z. Zou, J. Ye, K. Sayama, H. Arakawa, *Nature*, 2001, **414**, 625-627.

- 3 R. Asahi, T. Morikawa, T. Ohwaki, K. Aoki, Y. Taga, *Science*, 2001, **293**, 269-271.
- 4 W. Morales, M. Cason, O. Aina, N. R. de Tacconi, K. Rajeshwar, *J. Am. Chem. Soc.*, 2008, **130**, 6318-6319.
- 5 F. Qin, G. Li, R. Wang, J. Wu, H. Sun, R. Chen, *Chem. -Eur. J.*, 2012, **18**, 16491-16497.
- 6 H. Li, J. Shang, Z. Ai, L. Zhang, *J. Am. Chem. Soc.*, 2015, **137**, 6393-6399.
- 7 J. Xiong, G. Cheng, G. Li, F. Qin, R. Chen, *RSC Adv.*, 2011, **1**, 1542.
- 8 J. Y. Sheng, X. J. Li, Y. M. Xu, *ACS Catal.*, 2014, **4**, 732-737.
- 9 X. Ding, K. Zhao, L. Zhang, *Environ. Sci. Technol.*, 2014, **48**, 5823-31.
- 10 X. Zhang, Z. Ai, F. Jia, L. Zhang, *J. Phys. Chem. C*, 2008, **112**, 747-753.
- 11 H. Li, L. Zhang, *Nanoscale*, 2014, **6**, 7805-7810.
- 12 Z.-Q. Li, X.-T. Chen, Z.-L. Xue, *CrystEngComm*, 2013, **15**, 498.
- 13 M. Zhang, C. Shao, P. Zhang, C. Su, X. Zhang, P. Liang, Y. Sun, Y. Liu, *J. Hazard. Mater.*, 2012, **225-226**, 155-63.
- 14 M. Shang, W. Wang, J. Ren, S. Sun, L. Zhang, *Nanoscale*, 2011, **3**, 1474-1476.
- 15 T. Zhou, J. Hu, J. Li, *Appl. Catal., B: Environ.*, 2011, **110**, 221-230.
- 16 A. A. Alemi, R. Kashfi, B. Shabani, *J. Mol. Catal., A*, 2014, **392**, 290-298.
- 17 G. Tian, Y. Chen, R. Zhai, J. Zhou, W. Zhou, R. Wang, K. Pan, C. Tian, H. Fu, *J. Mater. Chem., A*, 2013, **1**, 6961.
- 18 Y. Chen, G. Tian, Y. Shi, Y. Xiao, H. Fu, *Appl. Catal., B: Environ.*, 2015, **164**, 40-47.
- 19 Q. C. Xu, Y. H. Ng, Y. Zhang, J. S. C. Loo, R. Amal, T. T. Y. Tan, *Chem. Commun.*, 2011, **47**, 8641-8643.
- 20 H.-i. Kim, J. Kim, W. Kim, W. Choi, *J. Phys. Chem. C*, 2011, **115**, 9797-9805.
- 21 H. Zhang, G. Chen, D. W. Bahnemann, *J. Mater. Chem.*, 2009, **19**, 5089-5121.
- 22 X. Lin, J. Xing, W. Wang, Z. Shan, F. Xu, F. Huang, *J. Phys. Chem. C*, 2007, **111**, 18288-18293.
- 23 M. Zhang, C. Shao, J. Mu, Z. Zhang, Z. Guo, P. Zhang, Y. Liu, *CrystEngComm*, 2012, **14**, 605.
- 24 P. Zhang, C. Shao, M. Zhang, Z. Guo, J. Mu, Z. Zhang, X. Zhang, Y. Liu, *J. Hazard. Mater.*, 2012, **217-218**, 422-8.
- 25 J. Zhang, Q. Xu, Z. Feng, M. Li, C. Li, *Angew. Chem., Int. Ed.*, 2008, **47**, 1766-9.
- 26 A. Hameed, T. Montini, V. Gombac, P. Fornasiero, *J. Am. Chem. Soc.*, 2008, **130**, 9658-9659.
- 27 J. Ren, W. Wang, M. Shang, S. Sun, E. Gao, *ACS Appl. Mater. Interfaces*, 2011, **3**, 2529-33.
- 28 F. Qin, H. Zhao, G. Li, H. Yang, J. Li, R. Wang, Y. Liu, J. Hu, H. Sun, R. Chen, *Nanoscale*, 2014, **6**, 5402-5409.
- 29 C. Kongmark, R. Coulter, S. Cristol, A. Rubbens, C. Pirovano, A. Löfberg, G. Sankar, W. van Beek, E. Bordes-Richard, R.-N. Vannier, *Cryst. Growth Des.*, 2012, **12**, 5994-6003.
- 30 F. D. Hardcastle, I. E. Wachs, *J. Raman. Spectrosc.*, 1990, **21**, 683-691.
- 31 L. Guy, M. Denis, *J. Raman. Spectrosc.*, 2006, **37**, 189-201.
- 32 J. C. Sczancoski, L. S. Cavalcante, N. L. Marana, R. O. da Silva, R. L. Tranquilin, M. R. Joya, P. S. Pizani, J. A. Varela, J. R. Sambrano, M. Siu Li, E. Longo, J. Andrés, *Curr. Appl. Phys.*, 2010, **10**, 614-624.
- 33 D. Machon, K. Friese, T. Brezowski, A. Grzechnik, *J. Solid State Chem.*, 2010, **183**, 2558-2564.
- 34 J. G. Choi, L. T. Thompson, *Appl. Surf. Sci.*, 1996, **93**, 143-149.
- 35 B. Brox, I. Olefjord, *Surf. Interface Anal.*, 1988, **13**, 3-6.
- 36 L. Benoist, D. Gonbeau, G. Pfister-Guillouzo, E. Schmidt, G. Meunier, A. Levasseur, *Surf. Interface Anal.*, 1994, **22**, 206-210.
- 37 S. Sajjad, S. A. K. Leghari, F. Chen, J. Zhang, *Chem. Eur. J.*, 2010, **16**, 13795-13804.
- 38 K. Qi, X. Chen, Y. Liu, J. H. Xin, C. L. Mak, W. A. Daoud, *J. Mater. Chem.*, 2007, **17**, 3504-3508.
- 39 X. Zhou, B. Jin, L. Li, F. Peng, H. Wang, H. Yu, Y. Fang, *J. Mater. Chem.*, 2012, **22**, 17900-17905.
- 40 L.-W. Zhang, H.-B. Fu, Y.-F. Zhu, *Adv. Funct. Mater.*, 2008, **18**, 2180-2189.
- 41 F. Zhou, R. Shi, Y. Zhu, *J. Mol. Catal., A*, 2011, **340**, 77-82.
- 42 A. Ishikawa, T. Takata, J. N. Kondo, M. Hara, H. Kobayashi, K. Domen, *J. Am. Chem. Soc.*, 2002, **124**, 13547-13553.
- 43 J.-P. Zou, S.-L. Luo, L.-Z. Zhang, J. Ma, S.-L. Lei, L.-S. Zhang, X.-B. Luo, Y. Luo, G.-S. Zeng, C.-T. Au, *Appl. Catal., B: Environ.*, 2013, **140-141**, 608-618.
- 44 Y. Peng, M. Yan, Q.-G. Chen, C.-M. Fan, H.-Y. Zhou, A.-W. Xu, *J. Mater. Chem., A*, 2014, **2**, 8517.